

Improved limit on the electric dipole moment of the electron

ACME Collaboration*

The standard model of particle physics accurately describes all particle physics measurements made so far in the laboratory. However, it is unable to answer many questions that arise from cosmological observations, such as the nature of dark matter and why matter dominates over antimatter throughout the Universe. Theories that contain particles and interactions beyond the standard model, such as models that incorporate supersymmetry, may explain these phenomena. Such particles appear in the vacuum and interact with common particles to modify their properties. For example, the existence of very massive particles whose interactions violate time-reversal symmetry, which could explain the cosmological matter–antimatter asymmetry, can give rise to an electric dipole moment along the spin axis of the electron. No electric dipole moments of fundamental particles have been observed. However, dipole moments only slightly smaller than the current experimental bounds have been predicted to arise from particles more massive than any known to exist. Here we present an improved experimental limit on the electric dipole moment of the electron, obtained by measuring the electron spin precession in a superposition of quantum states of electrons subjected to a huge intramolecular electric field. The sensitivity of our measurement is more than one order of magnitude better than any previous measurement. This result implies that a broad class of conjectured particles, if they exist and time-reversal symmetry is maximally violated, have masses that greatly exceed what can be measured directly at the Large Hadron Collider.

The electric dipole moment (EDM) of the electron is an asymmetric charge distribution along the particle's spin. The existence of an EDM requires violation of time-reversal symmetry. The standard model of particle physics predicts that the electron has such an EDM, d_e , but with a magnitude far below current experimental sensitivities^{1–3}. However, theories of physics beyond the standard model generally include new particles and interactions that can break time-reversal symmetry. If these new particles have masses of 1–100 TeV c^{-2} , theories typically predict that $d_e \approx 10^{-27}–10^{-30} e \text{ cm}$ ($1 \text{ cm} = 1.6 \times 10^{-21} \text{ C m}$, where e is the electron charge)^{4–8}—a value that is orders of magnitude larger than the standard model predictions, which is now accessible by experiment^{1,9}. Here we report the result of the ACME II experiment, an improved measurement of d_e with sensitivity over 10 times better than the previous best measurement, ACME I^{1,9}. This was achieved by improving the state preparation, experimental geometry, fluorescence collection and control of systematic uncertainties. Our measurement, $d_e = (4.3 \pm 3.1_{\text{stat}} \pm 2.6_{\text{syst}}) \times 10^{-30} e \text{ cm}$ ('stat', statistical uncertainty; 'syst', systematic uncertainty), is consistent with zero and corresponds to an upper limit of $|d_e| < 1.1 \times 10^{-29} e \text{ cm}$ at 90% confidence. This result constrains new time-reversal-symmetry-violating physics for broad classes of proposed beyond-standard-model particles with masses in the range 3–30 TeV c^{-2} .

Recent advances in the measurement of d_e ^{1,10–12} have relied on using the exceptionally high internal effective electric field (\mathcal{E}_{eff}) of heavy polar molecules^{13–15}. This gives rise to an energy shift $U = -\mathbf{d}_e \cdot \mathbf{E}_{\text{eff}}$, where $\mathbf{d}_e = d_e \mathbf{s}/(\hbar/2)$, \mathbf{s} is the spin of the electron and \hbar is the reduced Planck constant. The $H^3\Delta_1$ electronic state in the thorium monoxide (ThO) molecule has^{16,17} $\mathcal{E}_{\text{eff}} \approx 78 \text{ GV cm}^{-1}$ when the molecule is fully polarized; this requires only a very modest electric field ($\mathcal{E} \gtrsim 1 \text{ V cm}^{-1}$) applied in the laboratory. ACME I used ThO to place a limit of $|d_e| < 9.4 \times 10^{-29} e \text{ cm}$ (90% confidence)^{1,9}, which was recently confirmed by an experiment with trapped HfF⁺ molecular ions¹², which found $|d_e| < 1.3 \times 10^{-28} e \text{ cm}$.

An EDM measurement with thorium monoxide

As in ACME I, we performed our measurement in the $J = 1, M = \pm 1$ sublevels of the $H^3\Delta_1$ state of ThO, where J is the angular momentum and M is its projection along a quantization axis \hat{z} (Fig. 1a). In our applied electric field $\mathcal{E} = \mathcal{E}_z \hat{z}$, these states are fully polarized¹⁸, such that the internuclear axis \hat{n} , which points from the oxygen to the thorium nucleus, is either aligned or antialigned with \mathcal{E} . The direction of \hat{n} coincides with the direction of the field \mathcal{E}_{eff} that acts on \mathbf{d}_e . States with opposite molecule orientation are described by the quantum number $\tilde{N} = \text{sgn}(\mathcal{E} \cdot \hat{n}) = \pm 1$. The direction of \mathcal{E}_{eff} can be reversed either by reversing the laboratory field \mathcal{E} or by changing the state $\tilde{N} = \pm 1$ used in the measurement; each of these approaches allows us to reject a wide range of systematic errors^{19–21}.

The electron spin, \mathbf{s} , is along the spin of the molecular state, \mathbf{S} . We measure the energy difference between states with $M = \pm 1$ (which correspond to \mathbf{S} being aligned or antialigned with \mathcal{E}_{eff} ; Fig. 1a), which contains a term proportional to U . To do so, we prepare an initial coherent superposition of $M = \pm 1$ states, which corresponds to the spin \mathbf{S} being aligned with a fixed direction in the x – y plane (Fig. 2). The applied magnetic field, $\mathcal{B} = \mathcal{B}_z \hat{z}$, and \mathcal{E}_{eff} exert torques on the magnetic and electric dipole moments associated with the spin, causing \mathbf{S} to precess in the x – y plane by an angle ϕ as the molecules travel freely. The final value of ϕ is measured by laser excitation of the molecules, which induces fluorescence with a strength that depends on the angle between \mathbf{S} and the laser polarization. The angle ϕ is given by

$$\phi \approx \frac{-(\mu \tilde{\mathcal{B}} |\mathcal{B}_z| + \tilde{N} \tilde{\mathcal{E}} d_e \mathcal{E}_{\text{eff}}) \tau}{\hbar} \quad (1)$$

where $|\mathcal{B}_z| = |\mathcal{B} \cdot \hat{z}|$, $\tilde{\mathcal{B}} = \text{sgn}(\mathcal{B} \cdot \hat{z})$, $\tilde{\mathcal{E}} = \text{sgn}(\mathcal{E} \cdot \hat{z})$, τ is the spin precession time and $\mu = \mu_B g_{\mathcal{N}}$, where $g_{\mathcal{N}} = -0.0044$ is the g -factor of the $|H, J = 1, \mathcal{N}\rangle$ state²² and μ_B is the Bohr magneton. The sign, $\tilde{N} \tilde{\mathcal{E}}$, of the EDM contribution to the angle is given by the sign of the torque of \mathcal{E}_{eff}

*A list of participants and their affiliations appears at the end of the paper.

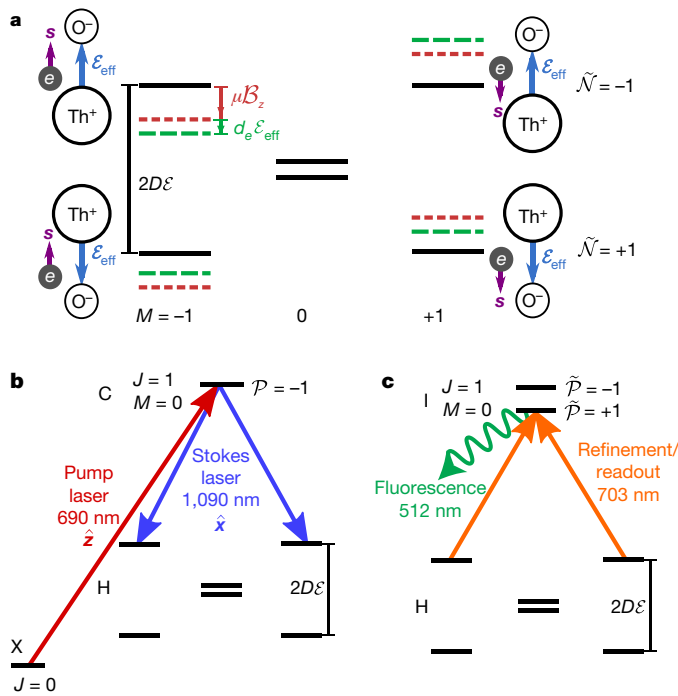


Fig. 1 | Energy levels of thorium monoxide and laser transitions. The addressed transitions are shown for one of several possible experimental states. **a**, Levels of the state H, $J=1$ in external electric (\mathcal{E}) and magnetic (\mathcal{B}) fields. The orientation of the effective electric field, \mathcal{E}_{eff} , is shown by blue arrows and that of the spin of the electron, \mathbf{s} , by purple arrows. The energy shifts $\mu\mathcal{B}_z$ (brown) and $d_e\mathcal{E}_{\text{eff}}$ (green) due to the magnetic moment μ and the EDM d_e , respectively, are shown. The $\tilde{N}=\pm 1$ states are split by $2D\mathcal{E} \approx 200$ MHz owing to the Stark effect, where D is the H-state electric dipole moment. **b**, STIRAP efficiently transfers population from the ground state $|X, J=0\rangle$ to a spin-aligned superposition of one molecule orientation, $\tilde{N}=+1$ or $\tilde{N}=-1$ ($\tilde{N}=-1$ shown here). STIRAP uses two lasers, the pump laser (red arrow; X-C, 690 nm, polarized along \hat{z}) and the Stokes laser (blue arrows; C-H, 1,090 nm, polarized along \hat{x}). **c**, The refinement laser (orange) removes imperfections in the spin-aligned state prepared by STIRAP. The readout laser (orange) excites the molecule from its original orientation, $\tilde{N}=+1$ or $\tilde{N}=-1$ ($\tilde{N}=-1$ shown here), to an isolated $J=1, M=0$ level in state I. This state can have either parity, $\tilde{P}=+1$ or $\tilde{P}=-1$ ($\tilde{P}=+1$ shown here). The I state decays via spontaneous photon emission, and we detect the resulting fluorescence (green wavy arrow).

on \mathbf{s} . The spin precession frequency, $\omega=\phi/\tau$, is given by the energy shift between the $M=\pm 1$ states (divided by \hbar). The value of d_e is extracted from the change in ω that is correlated with the orientation of \mathcal{E}_{eff} in the laboratory frame, that is, with the product $\tilde{N}\mathcal{E}$. By denoting this correlated component as $\omega^{\tilde{N}\mathcal{E}}$, we obtain $d_e=-\hbar\omega^{\tilde{N}\mathcal{E}}/\mathcal{E}_{\text{eff}}$.

We produce ThO molecules in a cryogenic buffer gas beam source^{23–25}. The molecules pass through laser beams and are rotationally cooled, increasing the population of the lowest energy level (ground electronic state X, rotational level $J=0$) by a factor of 2.5. The ThO molecules then enter a magnetically shielded region where the EDM measurement is performed. The electric field \mathcal{E} is produced by a set of parallel plates and the magnetic field \mathcal{B} is generated by a current circulating through coils (Fig. 2). We prepare the desired initial spin state using stimulated Raman adiabatic passage (STIRAP), coherently transferring the molecules from the ground state $|X, J=0\rangle$ to a specific sublevel of the lowest rotational level, $J=1$, of the metastable (lifetime 2 ms)¹⁸ electronic $H^3\Delta_1$ state manifold²⁶ (Fig. 1b). This results in a coherent superposition of $M=\pm 1$ states. STIRAP is implemented through a pair of co-propagating laser beams (wavelengths of 690 nm and 1,090 nm) resonant with the electronic transitions X-C and C-H. These beams are partially spatially overlapped, travel vertically (along \hat{y}) and have linear polarizations along \hat{z} and \hat{x} , respectively. We choose

which \tilde{N} state to address by tuning the frequency of the H-C STIRAP laser. The technical details of the STIRAP implementation are given in a separate publication²⁶.

Imperfections in the STIRAP-prepared spin-aligned state can lead to systematic errors but are suppressed with the following method. After leaving the STIRAP region, the molecules enter a linearly polarized ‘refinement’ laser that optically pumps away the unwanted spin component and leaves behind a dark superposition of the two resonant $M=\pm 1$ sublevels²⁷ of H. The refinement laser is resonant with the H-I transition (wavelength 703 nm; Fig. 1c). Within the short-lived (lifetime 115 ns) electronic state I, there are two well resolved opposite-parity ($\tilde{P}=\pm 1$) states with $J=1$ and $M=0$ ^{28,29}. The refinement laser polarization is nominally aligned with the STIRAP-prepared spin \mathbf{S}_{ST} and addresses the $\tilde{P}=+1$ parity state in I. The resulting refined state, $|\psi(t=0), \tilde{N}\rangle$, has \mathbf{S} aligned with \hat{x} more accurately than the initial STIRAP-prepared state (Fig. 2).

Molecules travel over a distance of $L \approx 20$ cm (corresponding to $\tau \approx 1$ ms) so that \mathbf{S} precesses in the x - y plane by angle ϕ (given by equation (1)). This yields the molecular state at time $t=\tau$,

$$|\psi(t=\tau), \tilde{N}\rangle = \frac{e^{-i\phi}|M=+1, \tilde{N}\rangle - e^{+i\phi}|M=-1, \tilde{N}\rangle}{\sqrt{2}} \quad (2)$$

We measure ϕ by exciting the H-I transition with laser light linearly polarized along direction \hat{e} . This yields fluorescence signals with intensity S_e , which depends on the angle between \hat{e} and \mathbf{S} . To remove the effects of fluctuations in molecule number, we excite the molecules with two alternating orthogonal linear polarizations, $\hat{e}=\hat{X}, \hat{Y}$, by modulating \hat{e} sufficiently rapidly (period 5 μ s) so that each molecule is addressed by both polarizations as it flies through the laser beam²². We record the corresponding fluorescence signals S_X and S_Y from the decay of I to the ground state X (wavelength 512 nm; see Extended Data Fig. 1a). We then compute the asymmetry¹⁸

$$\mathcal{A} = \frac{S_X - S_Y}{S_X + S_Y} = \mathcal{C} \cos[2(\phi - \theta)] \quad (3)$$

where the contrast \mathcal{C} is $95\% \pm 2\%$ on average and \hat{X} is defined to be at an angle θ with respect to \hat{x} in the x - y plane (Fig. 2). This procedure amounts to a projective measurement of the molecule alignment onto both \hat{X} and \hat{Y} . We set $|\mathcal{B}_z|$ and θ such that $\phi - \theta \approx (\pi/4)(2n + 1)$ for integer n , so that the asymmetry is linearly proportional to small changes in ϕ and thus maximally sensitive to d_e . We measure \mathcal{C} by dithering θ between two nearby values, $\tilde{\theta} = \pm 1$, that differ by 0.2 rad.

When limited by shot noise, the uncertainty in the measured phase, $\delta\phi$, per unit of measurement time scales as the square root of the photo-electron detection rate²². Compared with ACME I, ACME II improves phase sensitivity by an order of magnitude by increasing the fraction of beam source molecules used in the measurement. The implementation of STIRAP, together with a redesigned rotational-cooling scheme, improves the state preparation efficiency by a factor of 12. The detected solid angle of the diverging molecular beam is increased by a factor of 7 by moving the source closer to the detection region and increasing the separation between the electric-field plates, the size of all laser beams and the openings of the molecular beam collimators. The photon collection efficiency is increased by a factor of 5 using a combination of detecting shorter-wavelength photons (512 nm in ACME II, compared with 690 nm in ACME I), for which the photomultiplier tubes (PMTs) have higher quantum efficiency, and by replacing fibre bundles with lower-loss solid glass light pipes to transfer light to the PMTs. Together, these improvements increase our photoelectron detection rate by a factor of about 400 over ACME I.

We performed repeated spin precession measurements under varying experimental conditions to (a) isolate the EDM phase from background phases and (b) search for and monitor possible systematic errors. Within a ‘block’ of data (Extended Data Fig. 1c) taken over 60 s, we performed four identical measurements of ϕ for each state in the

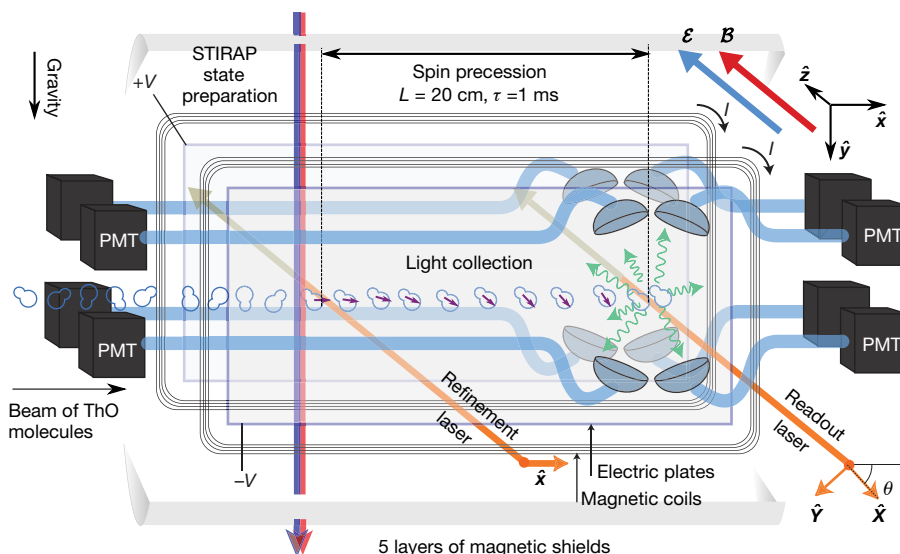


Fig. 2 | Schematic of the measurement region. A collimated pulse of ThO molecules enters a magnetically shielded region. A uniform electric field \mathcal{E} is applied by a set of transparent parallel plates at voltage $(+V, -V)$, and a uniform magnetic field \mathcal{B} is applied by circulating a current I through coils. A spin state (purple arrows) aligned along \hat{x} , prepared by STIRAP (blue and red vertical arrows) and refined via an optical pumping laser beam polarized along \hat{x} (left orange arrow), precesses over a length of

$L \approx 20$ cm (time $\tau \approx 1$ ms) in the applied electric and magnetic fields. The final spin alignment direction is read out by a laser (right orange arrow) with rapidly alternating linear polarizations, $\hat{e} = \hat{X}, \hat{Y}$ (with $\hat{e} = \hat{X}$ at an angle θ with respect to \hat{x}). The resulting fluorescence (green wavy arrows), the intensity of which depends on the angle between the spin of the molecular state, S , and \hat{e} , is collected and detected using photomultiplier tubes (PMTs).

complete set of 2^4 experimental states derived from four binary switches: the molecular alignment, $\tilde{\mathcal{N}}$; the direction of the applied electric field, $\tilde{\mathcal{E}}$; the readout-laser polarization dither state, $\tilde{\theta}$; and the magnetic field direction, $\tilde{\mathcal{B}}$. We form ‘switch-parity components’ of the phase, which are combinations of the measured phases that are odd or even under the selected switch operations²¹. We denote the experimental parity of a quantity with a superscript, u , that lists all the switches under which the quantity has odd parity (the parity of the quantity is even for all switches not included in the superscript), and we use the superscript ‘nr’ to indicate that the quantity is even under all considered switches. For example, we extract d_e from the $\phi^{\mathcal{N}\mathcal{E}}$ component of the phase (see equation (1)), which is odd under the $\tilde{\mathcal{N}}$ and $\tilde{\mathcal{E}}$ switches and even under all other switches. We extract the precession time τ from the component of the phase that is odd under only the $\tilde{\mathcal{B}}$ switch, $\phi^{\mathcal{B}} = -\mu|\mathcal{B}_z|\tau/\hbar$, and use it to compute the frequency components $\omega^u = \phi^u/\tau$ that are odd under the chosen parity u .

On a slower timescale, we perform additional ‘superblock’ binary switches to suppress known systematic errors and to search for unknown ones (Extended Data Fig. 1d). These switches are: $\tilde{\mathcal{P}}$, the excited-state parity addressed by the readout laser; $\tilde{\mathcal{L}}$, the interchange of the supplies that apply voltage to the two electric-field plates; and $\tilde{\mathcal{R}}$, the rotation of the readout $\hat{X}-\hat{Y}$ polarization basis by $\pi/2$, $\theta \rightarrow \theta + \pi/2$. The $\tilde{\mathcal{P}}$ and $\tilde{\mathcal{R}}$ switches both interchange the role of \hat{X} and \hat{Y} and thus reject systematic errors associated with small changes in the power, profile or pointing of the readout laser beam when the polarization \hat{e} is changed. The $\tilde{\mathcal{L}}$ switch rejects systematic errors that are proportional to the offset voltage of the electric-field power supplies. To compute d_e , we extract from the 2^7 block and superblock states $\omega^{\mathcal{N}\mathcal{E}}$, the component of the frequency that is odd under $\tilde{\mathcal{N}}$ and $\tilde{\mathcal{E}}$ and even under all other switches.

The EDM dataset consists of about 20,000 blocks, taken over the course of about two months (Extended Data Fig. 1f). During the acquisition of this dataset, in addition to the 7 switches described above, we also varied the magnitude of the magnetic field as $|\mathcal{B}_z| = 0.7$ mG, 1.3 mG, 2.6 mG and 26 mG (corresponding to $|\phi| \approx \pi/160, 2\pi/160, 4\pi/160$ and $\pi/4$, respectively), and the magnitude of the electric field as $|\mathcal{E}_z| = 80$ V cm⁻¹ and 140 V cm⁻¹. 5% of the data were taken with $|\mathcal{B}_z| = 2.6$ mG; the rest were taken at $|\mathcal{B}_z| = 0.7$ mG, 1.3 mG and 26 mG in approximately equal amounts. Equal amounts of data were taken with each of the two

electric field magnitudes. The $\omega^{\mathcal{N}\mathcal{E}}$ values obtained by isolating the data under each of these parameter values are shown in Fig. 3c.

Statistics of the EDM dataset

During data acquisition, we average 25 molecular pulses together to form a ‘trace’ (Extended Data Fig. 1b) and record individual traces corresponding to each of the eight PMTs. We typically sum the photo-electron signals in the eight PMTs but also frequently check the spatial dependence of the fluorescence as a diagnostic. Within a trace, we compute \mathcal{A} for each polarization cycle (Extended Data Fig. 1a). We then average 20 cycles into a single ‘group’, with the uncertainty defined as the standard error in the mean of the group. The uncertainties of all groups are consistent with the level of shot noise in our photoelectron signals. We then use standard uncertainty propagation methods to compute the uncertainties from an entire superblock.

The scatter in the superblock data is found to be larger than that expected from group-level uncertainties. This noise is present in all switch-parity components. The excess noise in the precession frequency has one contribution that is proportional to the magnitude of the magnetic field and another that is independent of it; the latter component results in a reduced χ^2 of $\chi^2_r \approx 3$. Because our fastest switch, $\tilde{\mathcal{N}}$, does not remove such noise, it enters the measurement at timescales lower than 0.6 s. We observed an increase in this noise after switching to a different ablation laser. This suggests that this noise might be related to fluctuations in the ablation characteristics, which are known to be correlated with molecular beam properties such as flux and transverse velocity.

The second component of the excess noise increases the scatter of our superblock data to $\chi^2_r \approx 7$, but only for the largest applied magnetic field, $|\mathcal{B}_z| = 26$ mG. We verified through simulations and a direct measurement that this is consistent with about 0.05% shot-to-shot fluctuations in the mean longitudinal molecular velocity ($\langle v \rangle \approx 200$ m s⁻¹). Because the refinement and readout beams are fixed in space, variations in $\langle v \rangle$ change the precession time τ , which causes variations in the phase ϕ , which is proportional to $|\mathcal{B}_z|$ (for $d_e = 0$), as shown in equation (1). To reduce its effect, we acquired most of the data at lower magnetic fields, where the associated increase in χ^2_r is negligible.

To prevent experimenter bias, we performed a blind analysis by adding an unknown offset to $\omega^{\mathcal{N}\mathcal{E}}$. We revealed this offset only after the

data collection, data cuts and two independent error analyses were complete. Figure 3a, b shows the distribution of the ω^{NE} superblock data. The majority of the data are consistent with a Gaussian distribution, but with more points in the tails. We performed a robust M -estimator analysis³⁰ on bootstrapped^{31,32} sets of data to extract confidence intervals corresponding to 1σ (68% confidence). Because the noise that arises from fluctuations in the mean longitudinal velocity depends on $|\mathcal{B}_z|$, we performed separate M -estimator analyses on subsets of data with different $|\mathcal{B}_z|$ values and then combined the sets using standard uncertainty propagation methods.

Systematic error investigations

To search for possible sources of systematic error, we varied over 40 different experimental parameters over larger ranges than those typically used in the experiment (Extended Data Table 1) and measured their effect on ω^{NE} and the other parity components of both ω and \mathcal{C} . In particular, we varied a parameter P over a range ΔP and, by assuming a linear relation between P and ω^{NE} , determined the slope $S_p = \partial\omega^{\text{NE}}/\partial P$. Such data, taken with intentionally applied parameter imperfections (that is, P set to a non-zero value although its ideal value is zero), were used only for the determination of systematic shifts and uncertainties, and were not included in the EDM dataset.

We used these measured slopes to compute systematic shifts and uncertainties as follows. If S_p was either expected or observed to be non-zero, we measured the residual ambient deviation of P from its ideal value, dP , and computed an associated systematic shift $d\omega_p^{\text{NE}} = S_p dP$. The uncertainty in $d\omega_p^{\text{NE}}$ was calculated using standard error propagation methods using the uncertainties in the measured values of S_p and dP . All the shifts and uncertainties of this type are included in the final systematic error budget given in Table 1. If S_p was expected and observed to be consistent with zero, we did not apply a systematic correction associated with parameter P , but still computed an associated uncertainty. We include uncertainties of this type in the final systematic error budget in certain cases described below.

We identified several parameters that cause non-zero changes in ω^{NE} , which we discuss here. The first such contribution to systematic shifts arises from gradients of \mathcal{B}_z along the z and y axes, $(\partial\mathcal{B}_z/\partial z)^{\text{nr}}$ and $(\partial\mathcal{B}_z/\partial y)^{\text{nr}}$ (Extended Data Fig. 2b). We understand the non-zero slopes associated with this set of parameters, $S_{\partial\mathcal{B}_z/\partial z} = \partial\omega^{\text{NE}}/\partial(\partial\mathcal{B}_z/\partial z)$ and $S_{\partial\mathcal{B}_z/\partial y} = \partial\omega^{\text{NE}}/\partial(\partial\mathcal{B}_z/\partial y)$, as follows. Because the spin precession phase, ϕ , is proportional to \mathcal{B}_z (for $d_e = 0$; see equation (1)), a gradient $\partial\mathcal{B}_z/\partial z$ ($\partial\mathcal{B}_z/\partial y$), together with a translation of the centre of mass of the detected molecular beam along the direction of the gradient, dz_{cm} (dy_{cm}), can create a shift in the measured precession frequency, $d\omega \propto (\partial\mathcal{B}_z/\partial z)dz_{\text{cm}}$ ($d\omega \propto (\partial\mathcal{B}_z/\partial y)dy_{\text{cm}}$) (Extended Data Fig. 2a). We identified two separate effects that can cause such translations in our system: one that arises from a non-reversing electric field, \mathcal{E}^{nr} , and one that arises from gradients in such a field, $\partial\mathcal{E}^{\text{nr}}/\partial z$ and $\partial\mathcal{E}^{\text{nr}}/\partial y$. Both effects are associated with incomplete laser excitation, and each can occur in both the STIRAP and probe laser beams. As described in detail in Supplementary Information, the systematic error requires a non-zero value of the readout-laser detuning (Δ), and a non-zero value of the STIRAP two-photon detuning (δ).

For the EDM dataset, we minimized the magnitudes of both slopes, $S_{\partial\mathcal{B}_z/\partial z}$ and $S_{\partial\mathcal{B}_z/\partial y}$, by tuning the readout laser so that $\Delta = 0$ and the STIRAP lasers so that $\delta = 0$ (Extended Data Fig. 2a). The residual slopes under these optimized conditions were then measured by applying large values of $\partial\mathcal{B}_z/\partial z$ and $\partial\mathcal{B}_z/\partial y$ and were found to be consistent with zero. To ensure that the imperfections leading to non-zero values of these slopes (namely, a combination of δ , Δ , \mathcal{E}^{nr} , $\partial\mathcal{E}^{\text{nr}}/\partial z$ or $\partial\mathcal{E}^{\text{nr}}/\partial y$) did not drift to large values, these slopes were monitored at regular intervals throughout the EDM data collection (Extended Data Fig. 1e). Finally, the ambient values of $\partial\mathcal{B}_z/\partial z$ and $\partial\mathcal{B}_z/\partial y$ during the acquisition of the EDM dataset were minimized to less than $1\text{ }\mu\text{G cm}^{-1}$ using the magnetic-field coils (Fig. 2). These field gradients were monitored twice daily using in situ magnetometers near the molecular beam; additional offline measurements were made before

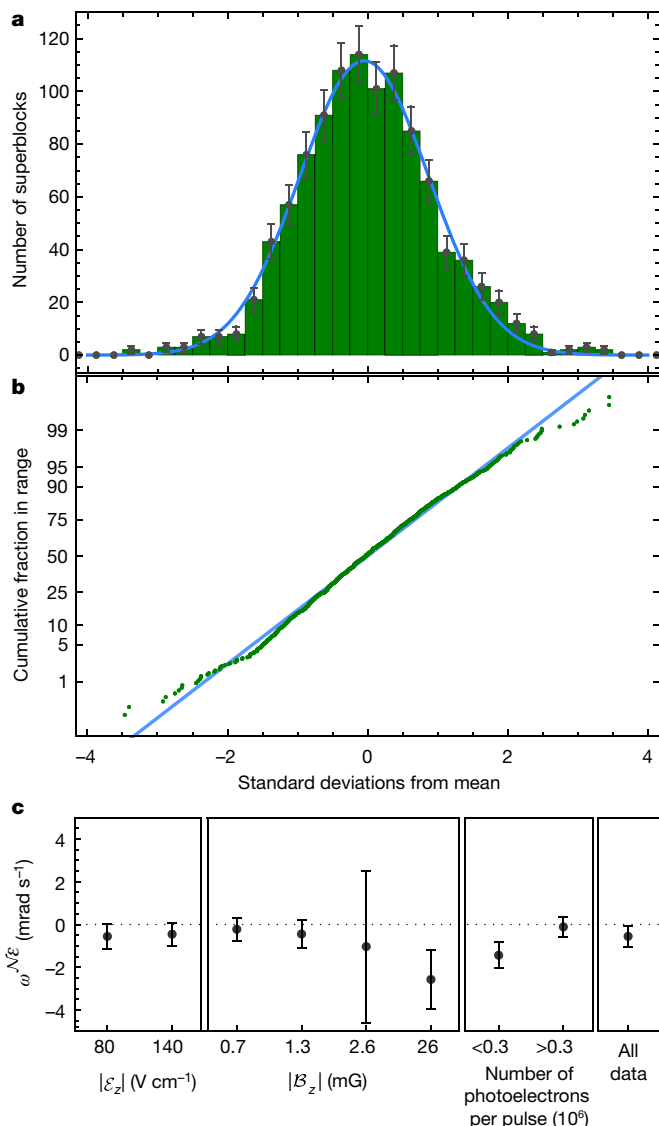


Fig. 3 | Statistics of the EDM dataset. **a**, Histogram of centred and normalized ω^{NE} superblock values, that is, $(\omega^{\text{NE}} - \langle \omega^{\text{NE}} \rangle)/\sigma_{\omega^{\text{NE}}}$. Here, $\langle \omega^{\text{NE}} \rangle$ is the mean of ω^{NE} over the dataset, $\sigma_{\omega^{\text{NE}}} = \sigma_{\omega^{\text{NE}}}^{\text{sn}}/\chi_r^2(\mathcal{B})$, where $\sigma_{\omega^{\text{NE}}}^{\text{sn}}$ is the superblock uncertainty propagated from ‘groups’ that is due to the shot noise, and $\chi_r^2(\mathcal{B})$ is the reduced χ^2 value for the sets of superblocks for a given magnetic-field magnitude. Error bars indicate the standard deviation in the bin expected from a Poisson distribution. The blue line shows a Gaussian fit to the histogram. **b**, Normal probability plot (green points) compared with a normal distribution (blue line). Deviations from the line outside $\pm 1.5\sigma$ indicate more data points in the tails of the distribution than expected from a normal distribution. **c**, Values of ω^{NE} , grouped according to $|\mathcal{E}_z|$, $|\mathcal{B}_z|$, the block-averaged number of photoelectrons per pulse, and combined for all states. Error bars correspond to 1σ (68% confidence interval).

and after the acquisition of the EDM dataset by translating the position of the magnetometers along the molecular beam path. We include in the systematic error budget (Table 1) a contribution calculated from the values of the measured systematic slope $S_{\partial\mathcal{B}_z/\partial z}$ ($S_{\partial\mathcal{B}_z/\partial y}$) and the ambient $\partial\mathcal{B}_z/\partial z$ ($\partial\mathcal{B}_z/\partial y$).

The next parameter that contributes to systematic shifts is associated with an ellipticity gradient across the spatial profile of the STIRAP H–C laser beam. In practice, we control the size of this ellipticity gradient by using a half-waveplate to change the angle, $\theta_{\text{ST}}^{\text{H–C}}$, between the original polarization of the H–C laser and the average birefringence axis. As described in detail in Supplementary Information, an ambient

Table 1 | Systematic shifts for $\omega^{\mathcal{N}\mathcal{E}}$ and their statistical uncertainties

Parameter	Shift	Uncertainty
$\partial B_z/\partial z$ and $\partial B_z/\partial y$	7	59
$\omega_{ST}^{\mathcal{N}\mathcal{E}}$ (via θ_{ST}^{H-C})	0	1
$P_{ref}^{\mathcal{N}\mathcal{E}}$	–	109
\mathcal{E}^{nr}	–56	140
$ \mathcal{C} ^{\mathcal{N}\mathcal{E}}$ and $ \mathcal{C} ^{\mathcal{N}\mathcal{E}B}$	77	125
$\omega^{\mathcal{E}}$ (via $B_z^{\mathcal{E}}$)	1	1
Other magnetic-field gradients (4)	–	134
Non-reversing magnetic field, B_z^{nr}	–	106
Transverse magnetic fields, B_x^{nr}, B_y^{nr}	–	92
Refinement- and readout-laser detunings	–	76
\mathcal{N} -correlated laser detuning, $\Delta^{\mathcal{N}}$	–	48
Total systematic	29	310
Statistical uncertainty		373
Total uncertainty		486

Values are shown in $\mu\text{rad s}^{-1}$. All uncertainties are added in quadrature. For $\mathcal{E}_{eff} = 78 \text{ GV cm}^{-1}$, $d_e = 10^{-30} e \text{ cm}$ corresponds to $|\omega^{\mathcal{N}\mathcal{E}}| = \mathcal{E}_{eff} d_e / \hbar = 119 \mu\text{rad s}^{-1}$.

birefringence gradient, in combination with a finite value of the refinement-laser beam attenuation, A_{ref} and a non-zero \mathcal{E}^{nr} leads to a non-zero value of $S_{\theta_{ST}^{H-C}} = \partial \omega^{\mathcal{N}\mathcal{E}} / \partial \theta_{ST}^{H-C} = (\partial \omega_{ST}^{\mathcal{N}\mathcal{E}} / \partial \theta_{ST}^{H-C}) / A_{ref}$.

Throughout the acquisition of the EDM dataset, we measured the slope $S_{\theta_{ST}^{H-C}}$ by applying a large θ_{ST}^{H-C} and measuring the value of $\omega^{\mathcal{N}\mathcal{E}}$ that survives refinement. This value is consistent with zero, directly bounding the attenuation under ordinary conditions to $A_{ref} > 10^4$. We measured the value of θ_{ST}^{H-C} with the following procedure. By tuning the power of the refinement laser, P_{ref} , to zero so that $A_{ref} = 1$, we observed a contribution to the precession frequency associated with the STIRAP state-preparation laser beams, ω_{ST} . Consistent with the ellipticity-gradient model described above, under these conditions we also observed an $\mathcal{N}\mathcal{E}$ -correlated component, $\omega_{ST}^{\mathcal{N}\mathcal{E}}$, resulting from the combination of a.c. Stark-shift effects and a non-zero $\delta^{\mathcal{N}\mathcal{E}}$ (caused by the residual ambient \mathcal{E}^{nr}). The slope $\partial \omega_{ST}^{\mathcal{N}\mathcal{E}} / \partial \theta_{ST}^{H-C}$ was calibrated by setting $P_{ref} = 0$ and measuring the dependence of $\omega_{ST}^{\mathcal{N}\mathcal{E}}$ on an exaggerated θ_{ST}^{H-C} . Finally, the value of θ_{ST}^{H-C} was found from the relation $\theta_{ST}^{H-C} = \omega_{ST}^{\mathcal{N}\mathcal{E}} / (\partial \omega_{ST}^{\mathcal{N}\mathcal{E}} / \partial \theta_{ST}^{H-C})$. To minimize the ellipticity gradient, we set θ_{ST}^{H-C} to the value that was found to minimize $\omega_{ST}^{\mathcal{N}\mathcal{E}}$. Both $\omega_{ST}^{\mathcal{N}\mathcal{E}}$ and the slope $S_{\theta_{ST}^{H-C}}$ were monitored at regular intervals throughout the acquisition of the EDM dataset (Extended Data Fig. 1e). The measured values of the systematic slope $S_{\theta_{ST}^{H-C}}$ and the residual θ_{ST}^{H-C} were used to compute the contribution of the STIRAP lasers to the systematic error budget (Table 1).

Another parameter that contributes to a systematic shift of $\omega^{\mathcal{N}\mathcal{E}}$ is an $\mathcal{N}\tilde{\mathcal{E}}$ -correlated component of the power of the refinement beam, defined by $P_{ref} = P_{ref}^{nr} + \tilde{\mathcal{N}}\tilde{\mathcal{E}}P_{ref}^{\mathcal{N}\mathcal{E}}$. As illustrated in Supplementary Information, a misalignment between the ϵ_{ref} and S_{ST} polarization vectors, θ_{ST}^{ref} , leads to a non-zero value in the slope $S_{P_{ref}^{\mathcal{N}\mathcal{E}}} = \partial \omega^{\mathcal{N}\mathcal{E}} / \partial P_{ref}^{\mathcal{N}\mathcal{E}}$.

For the EDM dataset, we minimized the magnitude of $S_{P_{ref}^{\mathcal{N}\mathcal{E}}}$ by tuning θ_{ST}^{ref} to zero via a half-waveplate in the refinement-laser beam. We did not observe clear evidence of a non-zero $P_{ref}^{\mathcal{N}\mathcal{E}}$ component in our EDM dataset. However, we put a limit on its possible size throughout the acquisition of the EDM dataset by placing bounds on the offset of $\omega^{\mathcal{N}\mathcal{E}B}$, which has a strong linear dependence on $P_{ref}^{\mathcal{N}\mathcal{E}}$ owing to a.c. Stark-shift effects^{1,9}. The $\partial \omega^{\mathcal{N}\mathcal{E}} / \partial P_{ref}^{\mathcal{N}\mathcal{E}}$ slope was monitored regularly throughout the acquisition of the EDM dataset (Extended Data Fig. 1e). We used the measured upper limit of $P_{ref}^{\mathcal{N}\mathcal{E}}$ and the value of $\partial \omega^{\mathcal{N}\mathcal{E}} / \partial P_{ref}^{\mathcal{N}\mathcal{E}}$ to calculate a contribution of $P_{ref}^{\mathcal{N}\mathcal{E}}$ to the systematic error budget (Table 1).

The next parameter that contributes to the systematic error budget is \mathcal{E}^{nr} , which has already been discussed as one of the parameters needed to induce the $\partial B_z/\partial z$ ($\partial B_z/\partial y$) and $\omega_{ST}^{\mathcal{N}\mathcal{E}}$ systematic effects. However, an additional contribution arises from imperfections in the

ellipticity gradients of the refinement and readout lasers in combination with \mathcal{E}^{nr} , which was one of the dominant systematic effects in ACME I^{1,9}. By applying a large value of \mathcal{E}^{nr} , we measured $S_{\mathcal{E}^{nr}} = \partial \omega^{\mathcal{N}\mathcal{E}} / \partial \mathcal{E}^{nr}$ regularly throughout the acquisition of the EDM dataset (Extended Data Fig. 1e). \mathcal{E}^{nr} and its gradients in the precession region, $\partial \mathcal{E}^{nr} / \partial z$ and $\partial \mathcal{E}^{nr} / \partial y$, were measured every two weeks during the acquisition of the EDM dataset using a mapping method based on microwave spectroscopy⁹. We include in the systematic error budget (Table 1) a contribution of this \mathcal{E}^{nr} systematic effect based on $S_{\mathcal{E}^{nr}}$ and the measured ambient \mathcal{E}^{nr} .

The next contribution to the systematic error arises from imperfections in the spin-measurement contrast, \mathcal{C} . As described in detail in Supplementary Information, we observed correlations $S_{|\mathcal{C}|^u} = \partial \omega^{\mathcal{N}\mathcal{E}} / \partial |\mathcal{C}|^u$ with two contrast channels, $|\mathcal{C}|^{\mathcal{N}\mathcal{E}}$ and $|\mathcal{C}|^{\mathcal{N}\mathcal{E}B}$. Although the average values $\langle |\mathcal{C}|^{\mathcal{N}\mathcal{E}} \rangle$ and $\langle |\mathcal{C}|^{\mathcal{N}\mathcal{E}B} \rangle$ of the corresponding contrast channels are consistent with zero in the EDM dataset, we include in our error budget a limit on their possible contributions extracted from $S_{|\mathcal{C}|^{\mathcal{N}\mathcal{E}}} (S_{|\mathcal{C}|^{\mathcal{N}\mathcal{E}B}})$ and $\langle |\mathcal{C}|^{\mathcal{N}\mathcal{E}} \rangle (\langle |\mathcal{C}|^{\mathcal{N}\mathcal{E}B} \rangle)$ (Table 1).

The last parameter observed to generate a systematic shift was $\omega^{\mathcal{E}}$, which can result from leakage-current, motional-magnetic-field ($\mathbf{v} \times \mathcal{E}$) and geometric-phase effects¹⁹. To measure the slope $S_{\omega^{\mathcal{E}}} = \partial \omega^{\mathcal{N}\mathcal{E}} / \partial \omega^{\mathcal{E}}$, we apply an \mathcal{N} -correlated component of the magnetic field, $B_z^{\mathcal{E}}$, which creates a large artificial $\omega^{\mathcal{E}}$. $S_{\omega^{\mathcal{E}}}$ is a measure of the suppression of any residual value of $\omega^{\mathcal{E}}$ by the \mathcal{N} switch^{20,21}. The mean value of $\omega^{\mathcal{E}}$ in the EDM dataset, $\langle \omega^{\mathcal{E}} \rangle$, was measured to be consistent with zero. We place a limit on the possible contributions from $\omega^{\mathcal{E}}$ effects using the measured values of $S_{\omega^{\mathcal{E}}}$ and $\langle \omega^{\mathcal{E}} \rangle$ (Table 1).

In addition to the above effects, we include in our systematic error budget possible contributions from the following parameters (all closely related to the parameters observed to cause a non-zero $\omega^{\mathcal{N}\mathcal{E}}$ shift in our measurement): residual (non-reversing) magnetic fields (along all three directions), all additional first-order magnetic-field gradients ($\partial B_x / \partial z, \partial B_y / \partial y, \partial B_y / \partial x, \partial B_z / \partial x$), refinement- and readout-laser detunings and the differential detuning between the two experimental \mathcal{N} states, $\Delta^{\mathcal{N}}$.

Results and conclusions

The result of this second-generation EDM measurement using ThO is $\omega^{\mathcal{N}\mathcal{E}} = -510 \pm 373_{\text{stat}} \pm 310_{\text{syst}} \mu\text{rad s}^{-1}$. Using $d_e = -\hbar \omega^{\mathcal{N}\mathcal{E}} / \mathcal{E}_{eff}$ and^{16,17} $\mathcal{E}_{eff} \approx 78 \text{ GV cm}^{-1}$ results in

$$d_e = (4.3 \pm 3.1_{\text{stat}} \pm 2.6_{\text{syst}}) \times 10^{-30} e \text{ cm} \quad (4)$$

where the combined statistical and systematic uncertainty, $\sigma_{d_e} = 4.0 \times 10^{-30} e \text{ cm}$, is a factor of 12 smaller than the previous best result, from ACME I^{1,9}.

An upper limit on $|d_e|$ is computed by applying the Feldman–Cousins prescription^{9,33} to a folded normal distribution, which yields

$$|d_e| < 1.1 \times 10^{-29} e \text{ cm} \quad (5)$$

at 90% confidence level. This is 8.6 times smaller than the best previous limit, from ACME I^{1,9}. Because paramagnetic molecules are sensitive to multiple time-reversal-symmetry-violating effects³⁴, our measurement can be more generally interpreted as $\hbar \omega^{\mathcal{N}\mathcal{E}} = -d_e \mathcal{E}_{eff} + W_S C_S$, where C_S is a dimensionless time-reversal-symmetry-violating electron–nucleon coupling parameter and $W_S = -2\pi\hbar / 282 \text{ kHz}$ is a molecule-specific constant^{16,17,35}. For the d_e limit given above, we assume $C_S = 0$. Assuming $d_e = 0$ instead gives $|C_S| < 7.3 \times 10^{-10}$ (90% confidence level).

Because the values of d_e and C_S predicted by the standard model are many orders of magnitude below our sensitivity^{2,3}, this measurement is a background-free probe for new physics beyond the standard model. Nearly every extension of the standard model^{4–6} introduces the possibility for new particles and new time-reversal-symmetry-violating phases, ϕ_T , that can lead to measurable EDMs. Within typical extensions of the standard model, an EDM arising from new particles

with rest-mass energy Λ in an n -loop Feynman diagram will have a size of^{8,14,36}

$$\frac{d_e}{e} \approx \kappa \left(\frac{\alpha_{\text{eff}}}{2\pi} \right)^n \left(\frac{m_e c^2}{\Lambda^2} \right) \sin(\phi_T) (\hbar c) \quad (6)$$

where α_{eff} ($\alpha_{\text{eff}} = 4/137$ for electroweak interactions) encodes the strength with which the electron couples to new particles, m_e is the electron mass and $\kappa \approx 0.1-1$ is a dimensionless prefactor whose value depends on the specific model of new physics. In typical models, where d_e is produced by one- or two-loop diagrams, for $\sin(\phi_T) \approx 1$ our result typically limits time-reversal-symmetry-violating new physics to energy scales above $\Lambda \approx 30$ TeV or $\Lambda \approx 3$ TeV, respectively⁴⁻⁸.

Online content

Any Methods, including any statements of data availability and Nature Research reporting summaries, along with any additional references and Source Data files, are available in the online version of the paper at <https://doi.org/10.1038/s41586-018-0599-8>.

Received: 12 June 2018; Accepted: 20 August 2018;
Published online 17 October 2018.

- Baron, J. et al. Order of magnitude smaller limit on the electric dipole moment of the electron. *Science* **343**, 269–272 (2014).
- Pospelov, M. E. & Khrapovich, I. B. Electric dipole moment of the W boson and the electron in the Kobayashi–Maskawa model. *Sov. J. Nucl. Phys.* **53**, 638–640 (1991).
- Pospelov, M. & Ritz, A. CKM benchmarks for electron electric dipole moment experiments. *Phys. Rev. D* **89**, 056006 (2014).
- Nakai, Y. & Reece, M. Electric dipole moments in natural super symmetry. *J. High Energy Phys.* **8**, 31 (2017).
- Barr, S. M. A review of CP violation in atoms. *Int. J. Mod. Phys. A* **08**, 209–236 (1993).
- Pospelov, M. & Ritz, A. Electric dipole moments as probes of new physics. *Ann. Phys.* **318**, 119–169 (2005).
- Engel, J., Ramsey-Musolf, M. J. & van Kolck, U. Electric dipole moments of nucleons, nuclei, and atoms: the standard model and beyond. *Prog. Part. Nucl. Phys.* **71**, 21–74 (2013).
- Bernreuther, W. & Suzuki, M. The electric dipole moment of the electron. *Rev. Mod. Phys.* **63**, 313–340 (1991).
- ACME Collaboration et al. Methods, analysis, and the treatment of systematic errors for the electron electric dipole moment search in thorium monoxide. *New J. Phys.* **19**, 073029 (2016).
- Hudson, J. J. et al. Improved measurement of the shape of the electron. *Nature* **473**, 493–496 (2011).
- Kara, D. M. et al. Measurement of the electron's electric dipole moment using YbF molecules: methods and data analysis. *New J. Phys.* **14**, 103051 (2012).
- Cairncross, W. B. et al. Precision measurement of the electron's electric dipole moment using trapped molecular ions. *Phys. Rev. Lett.* **119**, 153001 (2017).
- Sandars, P. G. H. The electric dipole moment of an atom. *Phys. Lett.* **14**, 194–196 (1965).
- Khrapovich, I. B. & Lamoreaux, S. K. *CP Violation Without Strangeness* (Springer, New York, 1997).
- Commins, E. D. & DeMille, D. in *Lepton Dipole Moments* (eds Roberts, B. L. & Marciano, W. J.) Ch. 14 (World Scientific, Singapore, 2010).
- Denis, M. & Fleig, T. In search of discrete symmetry violations beyond the standard model: thorium monoxide reloaded. *J. Chem. Phys.* **145**, 214307 (2016).
- Skripnikov, L. V. Combined 4-component and relativistic pseudo potential study of ThO for the electron electric dipole moment search. *J. Chem. Phys.* **145**, 214301 (2016).
- Vutha, A. C. et al. Search for the electric dipole moment of the electron with thorium monoxide. *J. Phys. B* **43**, 074007 (2010).
- Regan, B. C., Commins, E. D., Schmidt, C. J. & DeMille, D. New limit on the electron electric dipole moment. *Phys. Rev. Lett.* **88**, 071805 (2002).
- Bickman, S., Hamilton, P., Jiang, Y. & DeMille, D. Preparation and detection of states with simultaneous spin alignment and selectable molecular orientation in PbO. *Phys. Rev. A* **80**, 023418 (2009).

- Eckel, S., Hamilton, P., Kirilov, E., Smith, H. W. & DeMille, D. Search for the electron electric dipole moment using -doublet levels in PbO. *Phys. Rev. A* **87**, 052130 (2013).
- Kirilov, E. et al. Shot-noise-limited spin measurements in a pulsed molecular beam. *Phys. Rev. A* **88**, 013844 (2013).
- Hutzler, N. R., Lu, H. I. & Doyle, J. M. The buffer gas beam: an intense, cold, and slow source for atoms and molecules. *Chem. Rev.* **112**, 4803–4827 (2012).
- Hutzler, N. R. et al. A cryogenic beam of refractory, chemically reactive molecules with expansion cooling. *Phys. Chem. Chem. Phys.* **13**, 18976 (2011).
- Patterson, D. & Doyle, J. M. Bright, guided molecular beam with hydrodynamic enhancement. *J. Chem. Phys.* **126**, 154307 (2007).
- Panda, C. D. et al. Stimulated Raman adiabatic passage preparation of a coherent superposition of ThO $H^3\Delta_1$ states for an improved electron electric-dipole-moment measurement. *Phys. Rev. A* **93**, 052110 (2016).
- Gray, H. R., Whitley, R. M. & Stroud, C. R. Coherent trapping of atomic populations. *Opt. Lett.* **3**, 218–220 (1978).
- Kokkin, D. L., Steimle, T. C. & DeMille, D. Branching ratios and radiative lifetimes of the U, L, and i states of thorium oxide. *Phys. Rev. A* **90**, 062503 (2014).
- Kokkin, D. L., Steimle, T. C. & DeMille, D. Characterization of the $I(|\Omega| = 1) - X^1\Sigma^+(0, 0)$ band of thorium oxide. *Phys. Rev. A* **91**, 042508 (2015).
- Huber, P. J. Robust estimation of a location parameter. *Ann. Math. Stat.* **35**, 73–101 (1964).
- Efron, B. Bootstrap methods: another look at the jackknife. *Ann. Stat.* **7**, 1–26 (1979).
- Efron, B. & Tibshirani, R. Bootstrap Methods for standard errors, confidence intervals, and other measures of statistical accuracy. *Stat. Sci.* **1**, 54–75 (1986).
- Feldman, G. J. & Cousins, R. D. Unified approach to the classical statistical analysis of small signals. *Phys. Rev. D* **57**, 3873–3889 (1998).
- Kozlov, M. G. & Labzowsky, L. N. Parity violation effects in diatomic molecules. *J. Phys. B* **28**, 1933–1961 (1995).
- Dzuba, V. A., Flambaum, V. V. & Harabati, C. Relations between matrix elements of different weak interactions and interpretation of the parity-nonconserving and electron electric-dipole-moment measurements in atoms and molecules. *Phys. Rev. A* **84**, 052108 (2011).
- Fortson, N., Sandars, P. & Barr, S. The search for a permanent electric dipole moment. *Phys. Today* **56**, 33–39 (2003).

Acknowledgements This work was supported by the NSF. J.H. was supported by the Department of Defense. D.G.A. was partially supported by the Amherst College Kellogg University Fellowship. We thank M. Reece and M. Schwartz for discussions and S. Coteau, J. MacArthur and S. Sansone for technical support.

Reviewer information *Nature* thanks E. Hinds and Y. Shagam for their contribution to the peer review of this work.

Author contributions All authors contributed to one or more of the following areas: proposing, leading and running the experiment; design, construction, optimization and testing of the experimental apparatus and data acquisition system; setup and maintenance during the data runs; data analysis and extraction of physics results from measured traces; modelling and simulation of systematic errors; and the writing of this article. The corresponding authors are D.D., J.M.D. and G.G. (acme@physics.harvard.edu).

Competing interests The authors declare no competing interests.

Additional information

Extended data is available for this paper at <https://doi.org/10.1038/s41586-018-0599-8>.

Supplementary information is available for this paper at <https://doi.org/10.1038/s41586-018-0599-8>.

Reprints and permissions information is available at <http://www.nature.com/reprints>.

Publisher's note: Springer Nature remains neutral with regard to jurisdictional claims in published maps and institutional affiliations.

ACME Collaboration

V. Andreev^{1,5}, D. G. Ang¹, D. DeMille^{2,*}, J. M. Doyle^{1,*}, G. Gabrielse^{1,3,*}, J. Haefner¹, N. R. Hutzler^{1,4}, Z. Lasner², C. Meisenhelder¹, B. R. O'Leary², C. D. Panda¹, A. D. West^{2,6}, E. P. West^{1,6} & X. Wu^{1,2}

¹Department of Physics, Harvard University, Cambridge, MA, USA. ²Department of Physics, Yale University, New Haven, CT, USA. ³Center for Fundamental Physics, Northwestern University, Evanston, IL, USA. ⁴Division of Physics, Mathematics, and Astronomy, California Institute of Technology, Pasadena, CA, USA. ⁵Present address: Max Planck Institute of Quantum Optics, Garching, Germany. ⁶Present address: Department of Physics and Astronomy, UCLA, Los Angeles, CA, USA. *e-mail: acme@physics.harvard.edu

METHODS

Apparatus. To describe the experiment (and its imperfections) in detail, we define a coordinate system in which \hat{z} is the direction of the applied electric field (pointing from east to west in our laboratory), \hat{y} (which is along $\hat{z} \times \langle v \rangle$, where $\langle v \rangle$ is the average molecular velocity) points approximately downwards, and $\hat{x} = \hat{y} \times \hat{z}$ is approximately parallel to $\langle v \rangle$ (Fig. 2). This system is used throughout the main body of the article.

After leaving the beam source, the molecules have a thermal distribution of rotational states at 4 K and reside mostly (>70%) in the $J=0-2$ rotational levels. We use two stages of optical pumping for ‘rotational cooling’, namely, to enhance the population in the ground rotational level $|X, J=0, P=+1\rangle$. The first stage is performed in an electric field of about 0 V cm^{-1} , using 5–7 passes of a laser beam resonant with the $|X, J=2, P=+1\rangle \leftrightarrow |C, J=1, P=-1\rangle$ transition. Each pass has orthogonal polarization to the previous one, addressing all possible M states in $|X, J=2, P=+1\rangle$. Owing to the parity and angular momentum selection rules, this results in optical pumping of population from $|X, J=2, P=+1\rangle$ to $|X, J=0, P=+1\rangle$. The second stage is performed in an applied electric field of about 100 V cm^{-1} , which mixes the opposite-parity excited states $|C, J=1, P=\pm 1, M=\pm 1\rangle$. A multipass, alternating polarization laser beam drives the $|X, J=1, P=-1\rangle \leftrightarrow |C, J=1, P=\text{mixed}, M=\pm 1\rangle$ transition, partially transferring population from $|X, J=1\rangle$ to $|X, J=0\rangle$. These two combined rotational-cooling steps increase the population in the $|X, J=0\rangle$ state by a factor of 2.5.

The molecules then pass through fixed collimating apertures before entering the magnetically shielded spin precession region, where the \mathcal{B} and \mathcal{E} fields are applied. The electric field is produced by a pair of parallel fused silica plates coated with a thin layer (20 nm) of indium tin oxide (ITO) on one side and anti-reflection coating on the other side³⁷. The ITO-coated sides face each other with a gap of 45 mm between them and are connected to low-noise voltage supplies.

A spatial map of the electric-field magnitude was measured by performing microwave spectroscopy on the ThO molecules⁹. This measurement indicated that the non-reversing component of the electric field had a varying magnitude of $|\mathcal{E}^{\text{nr}}| \approx 1-5 \text{ mV cm}^{-1}$ at different points along the propagation direction of the molecular beam, x . We measured the spatial dependence of \mathcal{E}^{nr} in z and y by selectively blocking half of the STIRAP state-preparation and readout laser beams, respectively.

The vacuum chamber that houses the spin precession region is surrounded by five layers of mu-metal shielding. The coil design is optimized to create a uniform magnetic field along z . Additional coils allow us to apply magnetic-field offsets in the transverse directions (x and y), as well as all first-order gradients ($\partial \mathcal{B}_z / \partial z$, $\partial \mathcal{B}_z / \partial y$, $\partial \mathcal{B}_x / \partial x$, $\partial \mathcal{B}_y / \partial y$, $\partial \mathcal{B}_y / \partial x$, $\partial \mathcal{B}_z / \partial x$), for systematic error checks. The magnetic field is monitored by four three-axis fluxgate magnetometers, which are placed inside pockets inset in the vacuum chamber, 20–30 cm from the molecular beam. The electronic offset that is inherent to the fluxgate magnetometers is subtracted by rotating them in situ by 180°, and the position of each magnetometer can be translated along one axis. These magnetometers are used to infer changes in the magnetic field as well as information about its gradients. The magnetic field is also mapped before and after the acquisition of the EDM dataset by sliding a three-axis fluxgate magnetometer down the beamline (along \hat{x}) at the position of the molecules and at positions offset vertically (along \hat{y}). Measurement of the gradients along \hat{x} and \hat{y} , along with Maxwell’s equations, allow us to also infer the gradients along \hat{z} , where the mechanical geometry of the field plates prevent a direct measurement.

The STIRAP lasers travel vertically through the experimental setup, between the field plates. They are launched from the beamshaping optics at the top of the setup, which overlaps and focuses the two laser beams (waists of about $150 \mu\text{m}$) at the position of the molecular beam²⁶. The refinement and readout beams travel horizontally through the field plates, so all stages of the spin precession measurement are performed in a uniform electric field.

The STIRAP light originates from external cavity diode lasers (ECDLs) whose frequencies are locked to the resonance of an ultralow expansion glass (ULE) cavity. A linear drift of 7 kHz d^{-1} , due to the mechanical relaxation of the ULE spacer, is measured using a stabilized frequency comb and is corrected for using acousto-optic modulators (AOMs)²⁶. The refinement and readout lasers both derive from the same Ti:sapphire (Ti:S) laser (703 nm). We switch the Ti:S laser frequency between the two \tilde{N} states by tuning the length of the laser cavity using piezoelectric

elements. The Ti:S laser is locked to the ULE cavity via a transfer lock to a separate 703 nm ECDL. We address the two \tilde{P} states by shifting the frequency of the readout laser with the AOMs. Unlike in ACME I^{1,9}, a global rotation of both the refinement- and readout-laser polarizations, \tilde{G} , cannot be implemented because the spin alignment is already fixed by the polarization of the Stokes STIRAP laser to be nominally along \hat{x} ²⁶.

To normalize against the changing molecule number, we alternate the readout-laser polarization fast enough so that each molecule is reliably projected onto one of the two spin-alignment directions, with a probability determined by the orientation of its spin during its time of flight through the laser beam²². To do so, we overlap two laser beams with orthogonal \hat{X} and \hat{Y} polarizations, which we switch on and off rapidly using the AOMs. The \hat{X} and \hat{Y} pulses each have a duration of $1.9 \mu\text{s}$, with a $0.6 \mu\text{s}$ delay between them to minimize the overlap of signal due to the finite lifetime of the I state (115 ns)²⁹ between successive pulses (Extended Data Fig. 1a).

Fluorescence photons travel through the transparent field plates and are focused by one of eight lenses (four behind each field plate) into one of eight bent fused silica lightguides. Each lightguide carries the fluorescence photons to one of eight PMTs outside the magnetic shielding. The PMTs are optimized to detect fluorescence at 512 nm (approximately 25% quantum efficiency).

The PMT photocurrents are amplified and then recorded by a 14-bit digitizer operating at 16 million samples per second. All fast-timing (>10 Hz) electronics are controlled by a timing generator with jitter that is less than one sampling period of the digitizer. The digitizer signal is recorded by a computer, which communicates with a second computer that controls the slow switches (<10 Hz).

Statistics. The total run time for the collection of the EDM dataset was about 500 h; of these, about 350 h produced data that were used to compute the EDM and about 150 h were used for interleaved systematic-error checks (Extended Data Fig. 1). We also paused the experiment for about 8 h every 24 h (typically during the night) to thermally cycle the beam source to remove neon ice buildup.

Our robust M -estimator analysis^{30,32} was performed using different weighting functions, such as the Huber, Hampel and Tukey functions. To obtain the quoted results we used the Huber weighting function because of its simplicity and wide use; other choices would change the mean and its uncertainty by only a few per cent. This procedure also yields results consistent with those found using alternative methods, such as directly scaling the error bars by χ^2_r or forming the 5% trimmed mean of bootstrapped data³⁸. Although our d_e limit is computed using the Feldman–Cousins prescription^{9,33}, previous EDM experiments^{10,12,19} have reported limits based on a direct folded Gaussian distribution. To facilitate comparison with those experiments, we note that our limit computed in this way would be $|d_e| < 9.6 \times 10^{-30} e \text{ cm}$ (90% confidence level).

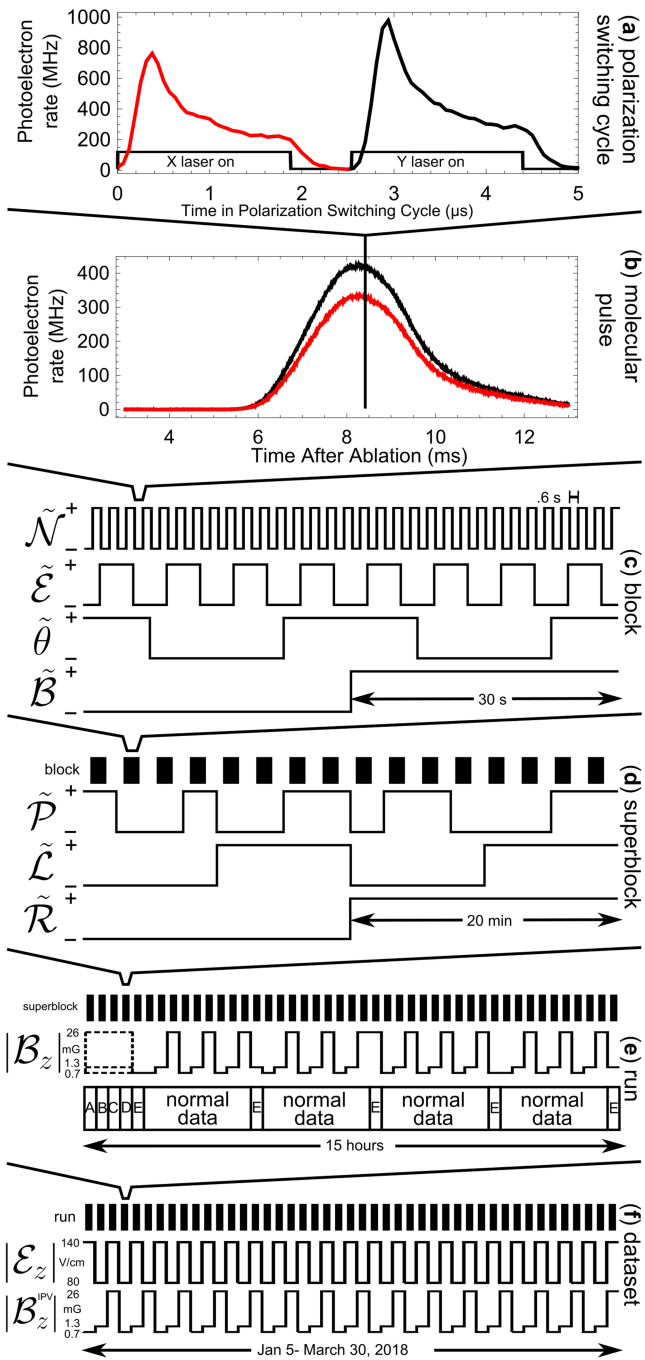
Future improvements. We believe that substantial improvements in sensitivity are possible with further development of the ACME technique. Detecting multiple photons from each molecule via optical cycling³⁹ could increase the experiment detection efficiency by an order of magnitude. Electric or magnetic focusing of the ThO molecular beam could increase the number of measured molecules by another order of magnitude, whereas improvements in cryogenic buffer-gas beam-source technology could give further gains. We are exploring various methods, such as faster switching between the addressed \tilde{N} states, to reduce the excess noise observed in ACME II. The dominant systematic errors that we observed can be further suppressed by improved magnetic-field control and reduced polarization gradients in the laser beams.

Code availability. The computer codes used for the analysis of the data are available from the corresponding authors on reasonable request.

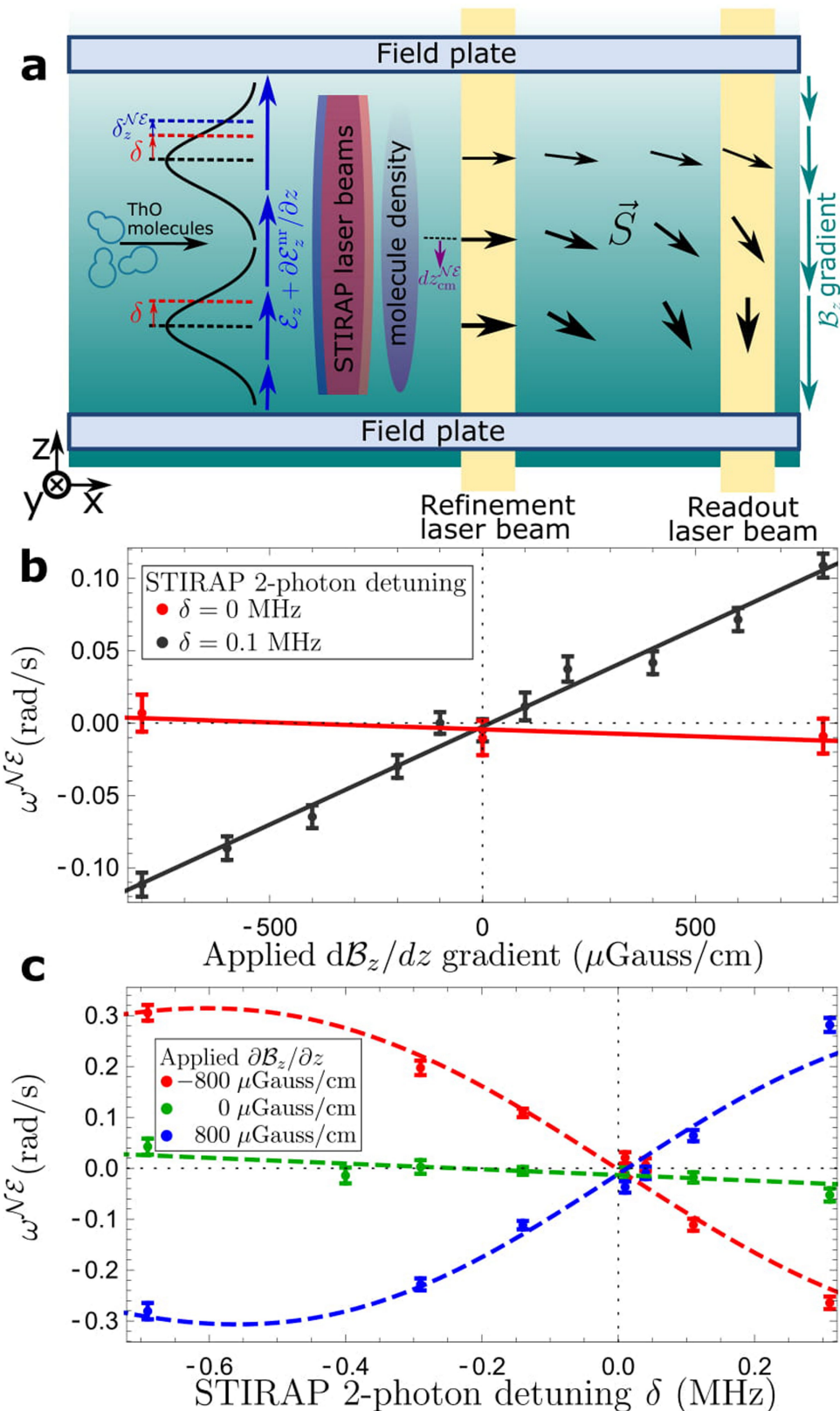
Data availability

The data that support the conclusions of this article are available from the corresponding authors on reasonable request.

37. Andreev, V., Panda, C. D., Hess, P. W., Spaun, B. & Gabrielse, G. A self-calibrating polarimeter to measure Stokes parameters. Preprint at <https://arxiv.org/abs/1703.00963> (2017).
38. Kenney, J. F. & Keeping, E. S. *Mathematics of Statistics: Part One* 4th edn (Chapman & Hall, London, 1954).
39. Shuman, E. S., Barry, J. F., Glenn, D. R. & DeMille, D. Radiative force from optical cycling on a diatomic molecule. *Phys. Rev. Lett.* **103**, 223001 (2009).



Extended Data Fig. 1 | Switching timescales. **a**, Fluorescence signal amplitude versus time in an \hat{X}, \hat{Y} polarization cycle. The red line corresponds to the signal from the \hat{X} -polarization laser and the black line to the signal from the \hat{Y} -polarization laser. **b**, Measured molecular trace (25 averaged pulses) versus time. Signal averaged over the entire \hat{X}, \hat{Y} polarization cycles shown in **a** are shown in red and black for the \hat{X} and \hat{Y} laser polarizations, respectively. **c**, Switches performed within a block. The \tilde{N} and $\tilde{\mathcal{B}}$ switches randomly alternate between a $(-+)$ and a $(+-)$ pattern, and the $\tilde{\mathcal{E}}$ and $\tilde{\theta}$ switches randomly alternate between $(-+ +)$ and $(+ - +)$ between blocks. **d**, Switches performed within a superblock. The $\tilde{\mathcal{P}}$ -state order is selected randomly, while $\tilde{\mathcal{L}}$ and $\tilde{\mathcal{R}}$ are deterministic. **e**, Run-data structure. We alternate between 'normal' EDM data, taken at three values of $|\mathcal{B}_z|$, and monitoring of known systematic effects by performing intentional parameter variations (IPVs). For several days data were taken with $|\mathcal{B}_z| = 2.6$ mG instead of $|\mathcal{B}_z| = 0.7$ mG, which is shown in the figure. Each IPV corresponds to one superblock, where a control parameter ($A-E$) is deliberately offset from its ideal value. Here, $A = P_{\text{ref}}$ (the refinement beam is completely blocked, to determine the intrinsic $\omega_{\text{ST}}^{\mathcal{N}\mathcal{E}}$), $B = \mathcal{E}^{\text{nr}}$, $C = P^{\mathcal{N}\mathcal{E}}$, $D = \phi_{\text{ST}}^{\mathcal{N}\mathcal{E}}$ and $E = \partial \mathcal{B}_z / \partial z$. The magnetic-field magnitude for the IPV of parameter E was varied between three experimental values within a run. **f**, The EDM dataset. The electric-field magnitude was varied from day to day. The magnetic-field magnitude for the IPVs for parameters A, B, C and D was varied between three experimental values.



Extended Data Fig. 2 | The $\partial\mathcal{B}_z/\partial z \times \delta \times \partial\mathcal{E}^{\text{nr}}/\partial z$ systematic error.
a, A $\partial\mathcal{E}^{\text{nr}}/\partial z$ gradient (blue arrows) causes a z -dependent two-photon detuning correlated with $\mathcal{N}\mathcal{E}$ ($\delta_z^{\mathcal{N}\mathcal{E}}$), due to the Stark shift $D\mathcal{E}$. When $\delta \neq 0$, the combination of a non-zero $\delta_z^{\mathcal{N}\mathcal{E}}$ and a dependence of the STIRAP efficiency on the two-photon detuning, $\partial\eta/\partial\delta$ (shown as black lines), acts to translate the detected molecular cloud (purple gradient ellipse) position by $dz_{\text{cm}}^{\mathcal{N}\mathcal{E}}$ (purple arrow). A non-zero $\partial\mathcal{B}_z/\partial z$ (teal-colour gradient) causes molecules to accumulate more (less) precession phase if their position has

a smaller (larger) z coordinate. The effects combine to create the dependence of $\omega^{\mathcal{N}\mathcal{E}}$ on $\partial\mathcal{B}_z/\partial z$. The scales are exaggerated for clarity. **b**, The effect of changing the STIRAP two-photon detuning, δ , on the $\omega^{\mathcal{N}\mathcal{E}}$ versus $\partial\mathcal{B}_z/\partial z$. We note that the slope $\partial\omega^{\mathcal{N}\mathcal{E}}/\partial(\partial\mathcal{B}_z/\partial z)$ is consistent with zero when δ is set to zero. **c**, Dependence of $\omega^{\mathcal{N}\mathcal{E}}$ on δ and $\partial\mathcal{B}_z/\partial z$. Fits (dashed curves) to a simple lineshape model (see Methods) show good agreement with the data. $\delta = 0$ is defined as the point where all curves cross. The error bars in **b** and **c** represent 1σ statistical uncertainties.

Extended Data Table 1 | Parameters varied in the search for systematic errors**Category I Parameters****Magnetic fields**

- \mathcal{B} -field gradients: $\frac{\partial \mathcal{B}_z}{\partial z}, \frac{\partial \mathcal{B}_z}{\partial y}, \frac{\partial \mathcal{B}_x}{\partial x}, \frac{\partial \mathcal{B}_y}{\partial y}, \frac{\partial \mathcal{B}_y}{\partial x}, \frac{\partial \mathcal{B}_z}{\partial x}$ (even and odd under $\tilde{\mathcal{B}}$)
- Non-reversing \mathcal{B} -field: $\mathcal{B}_z^{\text{nr}}$
- Transverse \mathcal{B} -fields: $\mathcal{B}_x, \mathcal{B}_y$ (even and odd under $\tilde{\mathcal{B}}$)
- $\tilde{\mathcal{E}}$ -correlated \mathcal{B} -field: $\mathcal{B}_z^{\mathcal{E}}$
(to measure suppression of possible $\phi^{\mathcal{E}}$ effects by the $\tilde{\mathcal{N}}$ switch)

Electric fields

- Non-reversing \mathcal{E} -field: \mathcal{E}^{nr}
- Field plate ground voltage offset

Laser detunings

- Detuning of refinement/readout lasers: $\Delta_{\text{ref}}, \Delta_{\text{read}}$
- 1-photon, 2-photon detuning of STIRAP lasers
- $\tilde{\mathcal{P}}$ -correlated detuning: $\Delta^{\mathcal{P}}$
- $\tilde{\mathcal{N}}$ -correlated detuning: $\Delta^{\mathcal{N}}$
- Detuning of rotational cooling lasers

Laser powers

- $\tilde{\mathcal{N}}\tilde{\mathcal{E}}$ -correlated power, $P^{\mathcal{N}\mathcal{E}}$
- Power of refinement/readout lasers: $P_{\text{prep}}, P_{\text{read}}$
- $\tilde{\mathcal{N}}$ -correlated power, $P^{\mathcal{N}}$
- $\tilde{\mathcal{P}}$ -correlated power, $P^{\mathcal{P}}$
- Readout \hat{X}, \hat{Y} -dependent laser power

Laser pointings/position along \hat{x}

- Pointing change of the refinement/readout lasers
- Readout \hat{X}, \hat{Y} -dependent laser pointing
- Position of refinement beam along \hat{x}

Laser polarization

- Polarization rotation of readout laser
- Readout polarization dither angle, θ
- Refinement/readout laser ellipticity

Molecular beam clipping

- Clipping of the molecular beam along \hat{y} and \hat{z}
(changes transverse velocity and position of the ensemble)

Category II Parameters**Experiment Timing**

- Readout \hat{X}, \hat{Y} polarization switching rate
- Allowed settling time between block switches

Analysis

- Signal size cuts, asymmetry magnitude cuts, contrast cuts
- Spatial dependence of fluorescence recorded by the eight PMTs
- Variation with time within the molecular pulse
- Variation with time within the \hat{X}, \hat{Y} polarization cycle
- Search for correlations with all ω, C switch-parity components
- Search for correlations with auxiliary monitored parameters
(\mathcal{B} -fields, laser powers and frequencies, vacuum pressure, environment and beam source pressures and temperatures)
- 4 analyses of the data

Category I, parameters that we vary far from their typical value during data collection. We directly measure or place limits on the error, which leads to a linear shift in $\omega^{\mathcal{N}\mathcal{E}}$. Category II, parameters for which all values are consistent with normal conditions of the experiment. These served as checks for the presence of unexpected systematic errors.